

Four-Terminal Perovskite/Copper Indium Gallium Selenide Tandem Solar Cells: Unveiling the Path to >27% in Power Conversion Efficiency

Thomas Feeney, Ihtez M. Hossain, Saba Gharibzadeh, Fabrizio Gota, Roja Singh, Paul Fassel,* Adrian Mertens, Ahmed Farag, Jan-Philipp Becker, Stefan Paetel, Erik Ahlswede, and Ulrich W. Paetzold*

Over the past decade, the impressive progress in power conversion efficiency (PCE) of organometallic halide perovskite solar cells (PSCs), coupled with their ready integration into tandem solar cells, has led them to approach PCEs of 30% for tandem solar cells with a silicon bottom subcell. However, the complementary technology of perovskite/copper indium gallium selenide (CIGS) tandem solar cells has been thus far unable to reach similar efficiency values. Herein, a further advance in the efficiency of 4T perovskite/CIGS tandems is demonstrated, increasing the PCE up to 27.3% via systematic optimization of the top semitransparent PSC. Improvements in light management through the optimization of anti-reflection coatings, coupled with the development of transparent conductive oxides that incur very low parasitic absorption are reported. It is revealed that both are crucial for maximizing efficiency and, by utilizing additional optical simulations, a detailed loss analysis that enables us to outline a path toward approaching 30% PCE for 4T perovskite/CIGS tandem devices is developed.

1. Introduction

Immense progress has been demonstrated in the field of thin-film perovskite solar cells (PSCs) over the past decade, with power conversion efficiencies (PCEs) of over 25% achieved in single-junction devices.^[1] Considering efficiency limitations imposed on single-junction photovoltaic (PV) device performance by the Shockley–Queisser limit, any further increase in PCE is most easily achieved by tandem device architecture.^[2–7] Due to the wide and tunable

bandgap of the perovskite absorber, these semitransparent PSCs are typically employed as the top subcell^[8] (≈ 1.55 – 1.85 eV bandgap) paired with narrow-bandgap silicon,^[3,6] copper indium gallium selenide (CIGS),^[2,5] CIS^[9] or tin–lead PSCs^[10–12] as the bottom subcell. Within the current state of the art, these tandem devices utilize either a two-terminal (2T) or a four-terminal (4T) architecture. A promising tertiary architecture known as three-terminal (3T) also exists and was demonstrated as feasible for perovskite-based tandems in 2019,^[13,14] but is currently in the inceptive period of research. 2T devices (also referred to as monolithic devices)^[2,3] involve a monolithic interconnection of the top and bottom subcells into a single PV device, leading to a simpler electrical connection as compared to 4T tandems. Furthermore, 2T devices omit additional

transparent conductive oxide (TCO) layers and often replace them with a dedicated recombination layer.^[2,3] However, they suffer from the requirement of current-matching between the two subcells for optimal function, imposing harsh restrictions on subcell thickness and bandgap.^[15] In comparison, 4T devices (also referred to as mechanically stacked devices)^[5–7] have a distinct benefit of independent fabrication of the two subcells, and do not require current matching. However, their integration into electrical systems is typically more complex, requiring two inverters in a PV system. One of

T. Feeney, I. M. Hossain, S. Gharibzadeh, R. Singh, P. Fassel, A. Farag, U. W. Paetzold
Light Technology Institute
Karlsruhe Institute of Technology
76131 Karlsruhe, Germany
E-mail: paul.fassel@kit.edu; ulrich.paetzold@kit.edu

 The ORCID identification number(s) for the author(s) of this article can be found under <https://doi.org/10.1002/solr.202200662>.

© 2022 The Authors. Solar RRL published by Wiley-VCH GmbH. This is an open access article under the terms of the Creative Commons Attribution-NonCommercial License, which permits use, distribution and reproduction in any medium, provided the original work is properly cited and is not used for commercial purposes.

DOI: 10.1002/solr.202200662

I. M. Hossain, S. Gharibzadeh, F. Gota, R. Singh, P. Fassel, A. Farag, U. W. Paetzold
Institute of Microstructure Technology
Karlsruhe Institute of Technology
76344 Eggenstein-Leopoldshafen, Germany

A. Mertens
Institute of Photonics and Quantum Electronics
Karlsruhe Institute of Technology
76131 Karlsruhe, Germany

J.-P. Becker, S. Paetel, E. Ahlswede
Zentrum für Sonnenenergie- und Wasserstoff-Forschung Baden-Württemberg (ZSW)
70563 Stuttgart, Germany

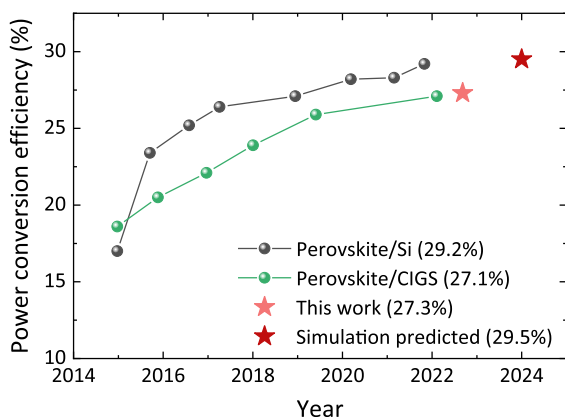


Figure 1. Historic development of the maximum reported power conversion efficiencies of 4T perovskite/Si and perovskite/CIGS tandem solar cells.^[5,17–25,27] Stars represent the performance of the prototype device developed in this work (27.3%) and the prediction after adopting the outlined recommendations in our optical simulations (29.5%).

the additional challenges of these 4T devices is the susceptibility to higher optical losses due to the requirement of the aforementioned additional TCO layer.^[7,16]

Impressive progress has been demonstrated over the past decade for the 4T architecture, with remarkable PCEs very close to 30% reported for perovskite-on-silicon (perovskite/Si) tandems. **Figure 1** outlines the historical development in maximum achieved PCE in each year for such devices, with the caveat that the stated PCEs have not been certified.^[5,17–25] By the end of 2019, both perovskite/Si and perovskite-on-CIGS (perovskite/CIGS) 4T tandems had reached PCEs above 25%,^[1–3,5,6] with the most recent record at the time of writing achieved by Solliance, who reported new PCEs of 29.2% and 27.1% in late 2021 for perovskite/Si and perovskite/CIGS respectively, with currently unstated device area or architecture.^[26] This achievement for 4T perovskite/CIGS tandem solar cells has recently been achieved a second time, with Zhang et al. obtaining a PCE of 27.1% in 2022.^[27] It is worth noting that perovskite tandems based on Si bottom solar cells have consistently presented higher PCEs compared to CIGS. One of the primary reasons for the superior performance is the higher near-infrared (NIR) response in the Si bottom subcell.^[17,28] However, CIGS possesses multiple inherent qualities distinct from silicon with the potential to enhance its applicability. These include bandgap tunability (≈ 1.0 – 1.7 eV),^[29] radiation hardness,^[30] and the possibility for lightweight flexible tandem devices.^[31] Moreover, it is important to note that perovskite/Si tandems have received significantly more research attention, as evidenced by the significant disparity in research articles that have been published on perovskite/Si in comparison to perovskite/CIGS (see Figure S1, Supporting Information). Therefore, notable room for improvement in the field of perovskite/CIGS tandem solar cells is both feasible and desirable.

Detailed-balance calculations yield theoretically achievable PCEs of up to 45% for two-junction tandem solar cells,^[32–34] while more recent applicable calculations, which incorporate material properties of the CIGS and perovskite subcells in various real-world situations, predict feasible PCEs of around 32%^[35]

indicating the extensive scope for further developments in PCE of perovskite/CIGS tandem solar cells. Improving the PCE of tandem devices that combine perovskites with established thin-film technologies can be accomplished via multiple methods. Increasing the PCE of the top semitransparent PSC (see historic development of the maximum reported PCE in the literature as well as that achieved in this work (18.5%) in Figure S2, Supporting Information) directly translates to 4T PCE, while improving the transmittance of NIR photons through the PSC device enhances 4T performance via increasing the bottom cell photocurrent. In this work, we systematically optimize the layer stack of the top semitransparent perovskite subcell, focusing on enhancing its optical properties to improve the PCE of both sub-cells, obtaining a new record PCE for 4T perovskite/CIGS tandem solar cells of 27.3%. The optimization focuses on light management by employing various TCOs with low parasitic absorption coupled with optimized anti-reflection coatings (ARCs) to reduce reflection losses. Finally, with the aid of optical simulations, we develop a detailed loss analysis to highlight the most promising methods to further improve PCE, with 4T perovskite/CIGS tandem PCEs approaching 30% considered feasible in the near future (Figure 1).

2. Results and Discussion

Optical losses in 4T perovskite/CIGS tandem solar cells arise from parasitic absorption and reflection losses.^[16,36–39] Not only do these losses lower the PCE of the top semitransparent PSC, but also limit sub-bandgap transmission of the photons through the perovskite top cell. The latter decreases current generation in the CIGS bottom solar cell and, hence, results in an overall reduction of the 4T tandem PCE. Though every active layer contributes in some form to parasitic absorption, the main contributors in a 4T tandem device are the two TCOs at the front and rear side of the top semitransparent perovskite subcell, where the front is defined as the first TCO exposed to incident light.^[16,39] In contrast, reflection losses are more complex, stemming from numerous interfaces in the tandem stack, for instance, air/glass, perovskite/charge transport layers, transparent conductive oxide/air, etc.^[28]

2.1. Optimization of Front and Rear TCOs

In our first optimization, we investigate three different combinations (Stack A, B, and C) for front and rear TCOs in a planar inverted semitransparent PSC stack with the aim of minimizing parasitic absorption, as visualized in the schemes in **Figure 2**, along with detailed optical properties from UV–Vis measurements. In all optical stacks, 2PACz is used as a hole transporting layer (HTL), C_{60}/SnO_x is the electron transporting layer (ETL) and the double-cation perovskite ($Cs_{0.17}FA_{0.83}Pb(I_{0.92}Br_{0.08})_3$) exhibits a bandgap of ≈ 1.62 eV. Stack A represents our reference stack, which typically uses tin-doped indium oxide (ITO) as both the TCOs. To reduce parasitic absorption losses, we first modify our stack by fabricating optical filters using in-house sputtered indium-doped zinc oxide (IZO) as a replacement for the rear ITO (Stack B in Figure 2). This was a clear first step in improving the NIR wavelength (800–1200 nm) optical properties of our stack as, according to previous studies, a rear ITO layer contributes significant parasitic absorption that can be readily reduced

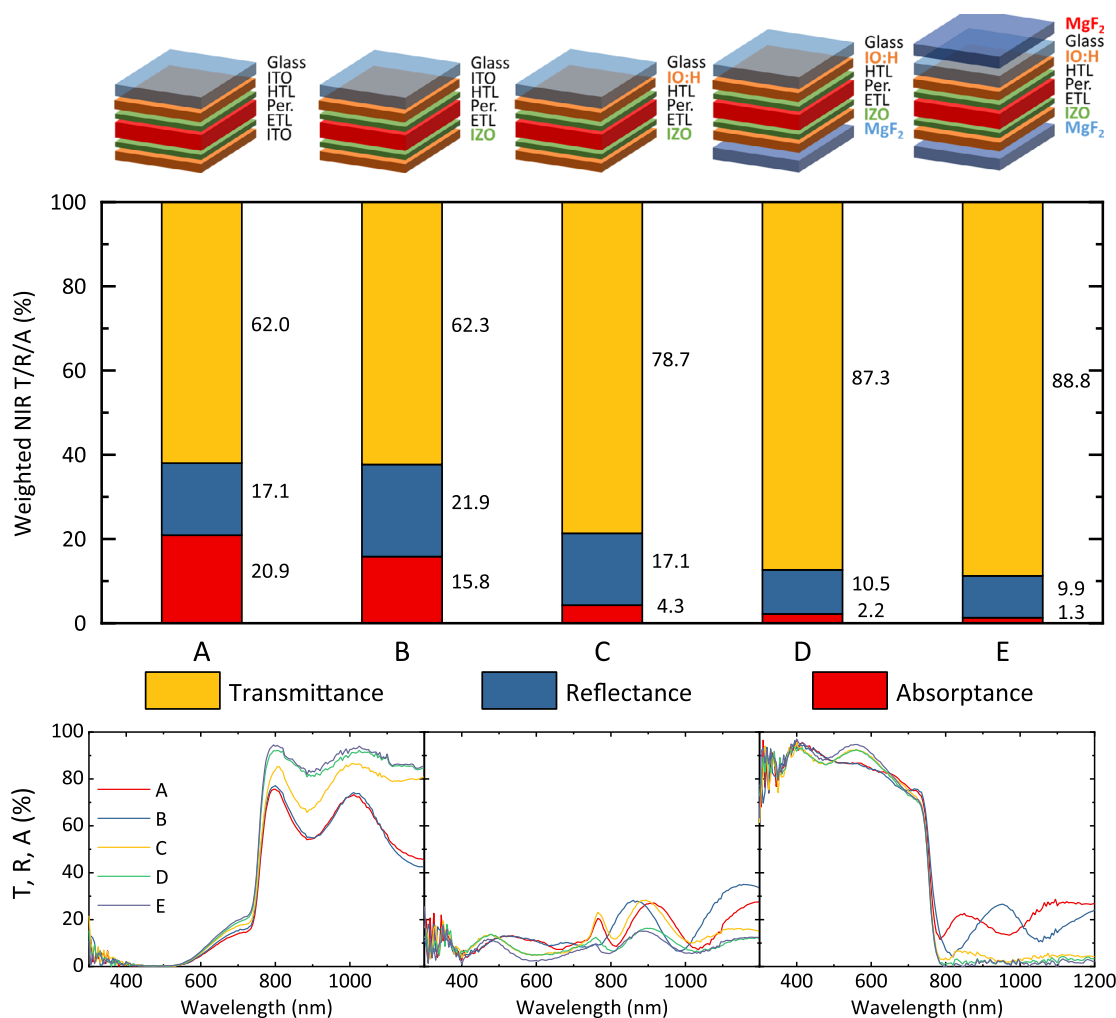


Figure 2. Schematic illustration of semitransparent perovskite solar cells (PSCs) with various layer configurations: i) Stack A uses tin-doped indium oxide (ITO) as both front and rear transparent conductive oxides (TCOs); ii) Stack B uses ITO as the front and indium-doped zinc oxide (IZO) as the rear TCO; iii) Stack C uses IO:H as the front and IZO as the rear TCO; iv) Stack D uses the same configuration as Stack C with an additional MgF_2 layer deposited on the rear IZO; v) Stack E also uses the same configuration as Stack C with MgF_2 deposited on the rear IZO as well as on the front glass substrate. Changes to Stack A, which is the reference stack, are highlighted with color. The accompanying bar chart represents the breakdown of absorbance, reflectance, and transmittance in near-infrared wavelengths (800–1200 nm) for each respective stack. Values have been weighted against the relative portion AM 1.5G spectrum to obtain a practical effective value. In all optical stacks, 2PACz is used as a hole transporting layer (HTL), while the electron transporting layer (ETL) is $\text{C}_{60}/\text{SnO}_x$. The results of the respective UV–vis measurements are presented underneath. From left to right: transmittance, reflectance, and absorbance.

by replacing it with IZO.^[16,21,40–42] Comparing Stack B with our reference Stack A, we observe an overall reduction in parasitic absorption of $\approx 5\%$. The parasitic absorption loss from the rear IZO could be reduced further by decreasing its thickness at the expense of increased sheet resistance, which, however, can have a detrimental effect on device performance. As this effect was greater than the gains in transmittance, we opted for an optimized IZO that exhibits lower sheet resistance ($\approx 45 \Omega \text{sq}^{-1}$) compared to the reference ITO discussed here, in addition to the aforementioned lower parasitic absorption. Further properties of these TCO electrodes can be found in Table S1, Supporting Information. We conduct additional analysis to elucidate the cause of the reduction in parasitic absorption using ellipsometry on TCOs deposited directly onto glass. Results

indicate that the reduction is associated with a decrease in the extinction coefficient (Figure S3, Supporting Information). A further comparison of these two stacks shows a notable increase in reflectance, which limits the overall enhancement in transmittance. This is due to increased Fresnel reflections which occur at the air/IZO (Stack B) interface in contrast to the air/ITO (Stack A) interface, caused by a higher refractive index for IZO in the NIR range (see Figure S3c, Supporting Information). Our later introduction of an ARC at the rear IZO/air interface will be tailored to minimize the impact of this effect.

Our second optimization explores the use of in-house sputtered hydrogenated indium oxide (IO:H) as an alternative to commercially available ITO as the front TCO to further reduce

the optical losses, especially in the NIR wavelengths (comparing Stack B and C in Figure 2).^[43–45] More details regarding the fabrication of IO:H can be found in our previous study.^[16] This replacement facilitates a substantial improvement in NIR transmittance of $\approx 16.5\%$ absolute, which we attribute to a reduction of both parasitic absorption ($\approx 11.5\%$) and reflection losses ($\approx 5\%$). The reduction in parasitic absorption is a result of a reduced extinction coefficient of IO:H (see Figure S3b, Supporting Information) from the presence of a low charge carrier concentration ($\approx 10^{20} \text{ cm}^{-3}$). The reduction in reflection losses due to the replacement of the front ITO with IO:H is a result of a considerably higher refractive index of IO:H, which is well matched to an optimum refractive index in the visible as well as NIR wavelength range (see Figure S3, Supporting Information). Here, the optimum refractive index implies the refractive index (determined from $n_{\text{optimum}} = \sqrt{n_{\text{glass}} n_{\text{perovskite}}}$) of an ideal medium, which would minimize the reflectance between glass and the perovskite absorber. In contrast to IO:H, the refractive index of the ITO decreases in the visible wavelengths and drops sharply in the NIR wavelengths, which is a result of a blue-shifted ITO plasma frequency (due to a high charge carrier concentration of magnitude $\approx 10^{21} \text{ cm}^{-3}$).^[46,47] Therefore, replacing the front ITO with IO:H significantly reduces both parasitic absorption as well as reflection loss to improve NIR transmittance.

2.2. Introduction of MgF₂ Antireflection Coating

In our third optimization series, in an effort to continue improving NIR transmittance and light in-coupling, we compare two configurations (Stacks D and E) incorporating additional layers of MgF₂ with the previous Stack C. One utilizes MgF₂ exclusively atop the rear IZO (see Figure 2, Stack D), while the other has MgF₂ deposited on both sides of the semitransparent PSC (see Figure 2, Stack E). Since MgF₂ exhibits a comparatively constant refractive index of ≈ 1.38 for a wide range of wavelengths,^[48] a value below both the rear IZO and front glass, it can be exploited as a suitable ARC for visible and NIR wavelengths, given appropriate layer thickness. Therefore, prior to incorporation into complete stacks, each layer thickness was optimized with respect to NIR transmission to maximize the resultant current obtained in the 4T tandem configuration. Further details on the optimization of the MgF₂ thickness are shown in Figures S4 and S5, Supporting Information. We demonstrate that even a 150 nm thick layer of MgF₂ deposited only on the rear side significantly reduces the IZO/air interface reflection, achieving an absolute improvement of $\approx 8.6\%$ in NIR transmittance. This improvement is essential for achieving high PCE in the bottom subcell of perovskite-based tandems. Employing another 125 nm thick MgF₂ layer at the front glass side (Stack E) further reduces the air/glass reflection loss by $\approx 0.5\%$. The resultant overall transmittance averages 88.8% over the spectrally relevant NIR range, with minimized reflectance and parasitic absorptance losses of 9.9% and 1.3%, respectively. Overall, these findings show the importance of implementing low-loss TCOs in conjunction with ARCs to reduce parasitic absorption and reflection losses.

2.3. Fabrication of 4T Perovskite/CIGS Tandem Solar Cells

To demonstrate the benefits of using top subcells with low optical loss, as achieved by our previous optimizations, on the performance of the perovskite/CIGS tandem solar cells, we fabricate top semitransparent PSCs with an active area of 10.5 mm². The layer stack of our optimized top semitransparent PSC is shown in Figure 3a and is sufficiently similar to the optical filters utilized for the optimization as presented in Stack E of Figure 2 such that any difference in overall optical properties can be disregarded when considering TCO and ARC optimizations. A 1 nm thick LiF layer is employed between the perovskite and the C₆₀ layer to reduce interfacial nonradiative recombination losses (charge carriers' lifetime increases from 68.5 to 277.4 ns when LiF is employed, see Figure S6, Supporting Information) and improve the open-circuit voltage (V_{OC}).^[49,50] The only difference between the device and optical filters is the presence of metallic Ag fingers, which form a C-shape to encircle the active area and thus reduce the series resistance in the rear contact of the semitransparent PSC. These metallic fingers will not influence the overall optical properties of the sample. For the calculation of the 4T tandem PCE, a CIGS solar cell was measured below a perovskite optical filter fabricated with the same layer sequence as the semitransparent PSC.

The current density–voltage (J – V) characteristics of the best performing semitransparent PSCs is presented in Figure 3b along with the standalone and filtered response of a 20.95% efficient CIGS bottom solar cell. The champion top semitransparent PSC demonstrates a PCE of 19.3% with a short-circuit current density (J_{SC}) of 20.7 mA cm⁻², a V_{OC} of 1.17 V, and a fill factor (FF) of 79% in the backward scan, while the filtered CIGS bottom cell exhibits a J_{SC} of 16.8 mA cm⁻², a V_{OC} of 0.66 V, and a FF of 78.6%. The latter represents an absolute drop of 30 mV in the bottom cell's V_{OC} compared to the unfiltered variants, which is comparable to the established literature.^[5,17–25] To demonstrate the benefit of using IO:H over ITO as a front TCO, semitransparent PSCs were also fabricated using a commercially available ITO as the front TCO. J – V , external quantum efficiency (EQE), and maximum power point (MPP) tracking measurements were carried out on both types of semitransparent PSCs that highlight the high yield and reproducibility and demonstrate a notable decrease in the EQE and the integrated J_{SC} for both the top and bottom devices in case of ITO (see Figure S7 and S8, Supporting Information). Full PV characteristics for semitransparent PSCs both with ITO and IO:H as front TCO as well as the respective results for filtered CIGS bottom cells are summarized in Table 1. For the semitransparent PSCs with a well-defined masked area, the stabilized PCE (obtained from MPP after 5 min under continuous AM1.5G illumination) is used to calculate their contribution to the 4T perovskite/CIGS tandem solar cell PCE. For the filtered CIGS bottom cells, due to the non-ideal spectrum of the solar simulator in the corresponding spectral region coupled with a lack of defined area, integrated J_{SC} values from EQE were used to calculate the PCE. An overall calculated 4T perovskite/CIGS tandem PCE of 25.2% is achieved using the ITO stack, slightly better than the values obtained in our previous study due to the use of IZO.^[7] The champion

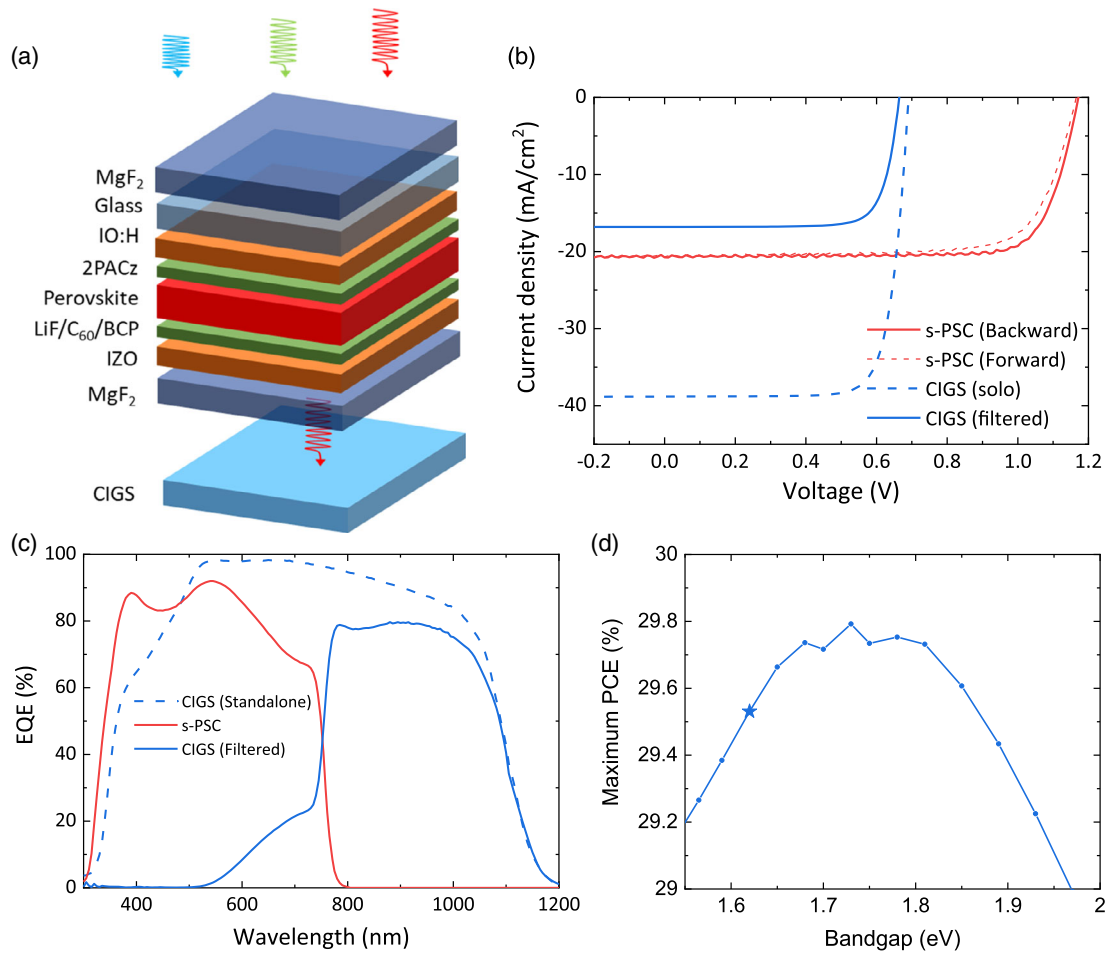


Figure 3. a) Schematic illustration of the layer stack for 4T perovskite/CIGS tandem solar cells. b) Current density–voltage (J – V) characteristics of the champion semitransparent PSC (reverse and forward scans), standalone and filtered CIGS solar cells. c) External quantum efficiency (EQE) of the champion semitransparent PSC and the standalone/filtered CIGS solar cell. The corresponding integrated short-circuit current densities are 19.6, 16.8, and 38.8 mA cm^{-2} , respectively. d) Simulation results indicating the maximum achievable power conversion efficiency (PCE) of a 4T perovskite/CIGS tandem solar cell with respect to variation in perovskite bandgap. At an optimal bandgap of ≈ 1.73 eV, the PCE is 29.8%, compared to 29.5% for the 1.62 eV bandgap perovskite utilized in this work, which is marked with a star (see Figure 4 for details regarding the optimization).

Table 1. Photovoltaic parameters of our champion top semitransparent PSCs with both ITO and IO:H as the front TCO, respectively, as well as that of the standalone/filtered CIGS solar cell. The stabilized PCE of the perovskite top and filtered bottom solar cells and the corresponding calculated 4T tandem PCE are given in bold. Average values for J – V parameters are presented in brackets.

Solar cell	Scan direction	V_{OC} [V]	J_{SC} [mA cm^{-2}]		FF [%]	PCE [%]	Stabilized PCE [%]
			Solar simulator	EQE			
Perovskite (ITO)	Reverse	1.16 (1.15)	19.8 (19.2)	18.8	80 (79)	18.4 (17.4)	17.5
	Forward	1.16 (1.15)	19.5 (19.1)		79 (75)	17.7 (16.4)	
Perovskite (IO:H)	Reverse	1.17 (1.15)	20.7 (21.5)	19.6	79 (70)	19.3 (17.1)	18.5
	Forward	1.17 (1.15)	20.9 (21.4)		76 (66)	18.5 (16.2)	
CIGS		0.69	42.3	38.8	78.2	20.95	20.95
CIGS (ITO filter)		0.66	15.5	14.7	78.5	7.7	7.7
CIGS (IO:H filter)		0.66	17.7	16.8	78.6	8.8	8.8
Perovskite/CIGS							27.3

4T perovskite/CIGS tandem solar cell in case of I:OH as front TCO exhibits a calculated PCE of 27.3%, with 18.5% stemming from the top semitransparent PSC and 8.8% derived from the filtered CIGS bottom device. The high PCE of the CIGS bottom solar cell is a result of high transmission achieved through the top semitransparent PSC due to our previous optimizations (see reflection, transmittance, and absorption spectra of the optical filter used for the champion device in Figure S9, Supporting Information). EQEs of both top and bottom cells are presented in Figure 3c, indicating high photon-to-current conversion, with an integrated J_{SC} within 6% of the J_{SC} obtained from the $J-V$ measurement.

In addition, we performed optical simulations of the maximum achievable PCE with respect to variation in perovskite bandgap for an optically optimized device stack. The details of this optimization are discussed in the next section. These simulations predict a 0.3% increase using a 1.73 eV bandgap given that the $V_{OC} \times FF$ ratio with respect to the Shockley–Queisser limit can be maintained, as shown in Figure 3c. However, due to complex factors that affect the performance of PSCs when increasing bandgap (such as increased voltage deficit, reduced stability, and halide migration), we elected to focus on PSCs with

1.62 eV bandgap in this work, which are known to create stable, high-efficiency devices.^[5,7]

3. Outlook

While employing the aforementioned approach adequately reduced optical losses, it remains possible to further improve the optical properties, and hence the resultant 4T perovskite/CIGS tandem solar cell PCE. To determine the potential scope of such optimizations, we performed optical simulations focusing on fine optimization of the relevant layers, without significantly altering the materials. **Figure 4a** outlines the effect of each additional modification or optimization. These can be broken down into thickness optimization of active layers, introduction of an encapsulation layer, and deployment of micro-textures to improve light in-coupling.^[36] Combined, these optimizations are shown to lead to an increase in PCE by an absolute 2.7%, thereby enabling 4T perovskite/CIGS tandem solar cell PCEs to approach 30%. For our optimizations, we first perform optical modeling and reproduce our experimental EQE data (see Figure S10, Supporting Information). Although there is a

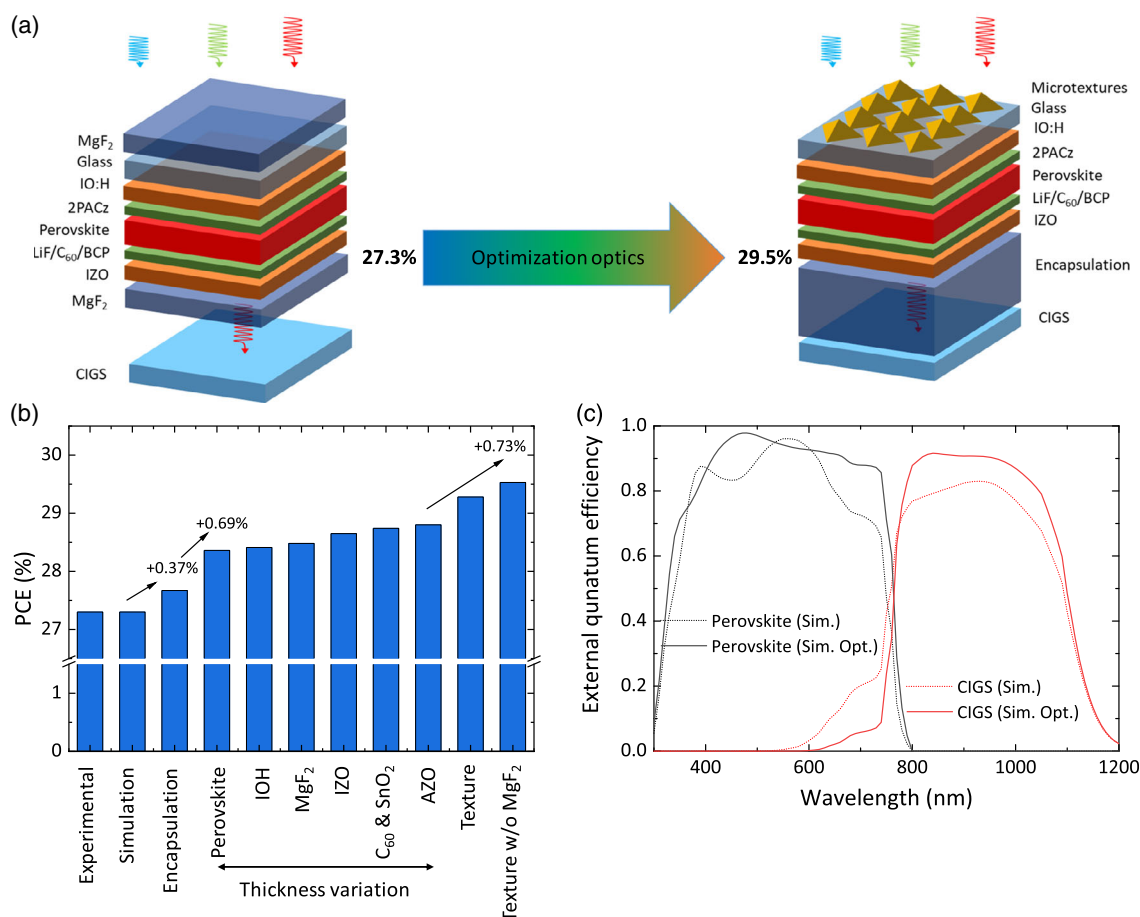


Figure 4. a) A schematic illustration of further modification to the 4T perovskite/CIGS tandem device to increase the device performance from 27.3% to up to 29.5%. b) Bar chart representing further modifications to individual layers, such as thickness optimizations of individual layers and the addition of an encapsulation layer and micro-textures. c) Simulated EQE of the optimized sub-cells for the 4T perovskite/CIGS tandem solar cell, resulting in an increase of PCE from 27.3% to 29.5%.

slight discrepancy between our simulated and the experimental EQE data, which we attribute to small variation of the actual thicknesses as well as the refractive indices and extinction coefficients of the layers, the final PCEs of 4T tandem devices (simulated and experimental) are the same (see Figure 4b). Using our simulation, we will show in the following how further optimizations reveal additional sources of improvement, and their expected magnitude. Thickness optimization of various layers (other than the perovskite absorber) leads to a minor improvement of $\approx 0.45\%$. In that regard, in Figure S11, Supporting Information, we exemplarily show the effect of changing the thickness of IO:H on its experimental sheet resistance (Figure S11a, Supporting Information) that could affect the V_{OC} and FF as well on the J_{SC} in both the top and bottom cell (Figure S11b,c, Supporting Information). Significant gains are only obtained when any of the following are introduced: 1) an encapsulation layer is introduced between the top and the bottom cell, 2) a thicker perovskite absorber is employed, and 3) micro-textures are deposited on the front glass substrate.

Though we have demonstrated that the presence of a layer of MgF_2 at the rear side can significantly reduce reflection losses, the air/ MgF_2 interfaces still incur notable reflections. Thus, an encapsulation layer (index matching layer) with a refractive index of ≈ 1.5 (optical data of ethylene-vinyl acetate (EVA) was employed for the simulations) would be beneficial to reduce interfacial reflections between the subcells and is expected to enhance the PCE by 0.37% (see Figure 4b). However, employing such an encapsulation layer is expected to introduce additional fabrication challenges, potentially impact stability, and increase the difficulty of obtaining proper contacts/terminals for the tandem device. The second aspect, calculated to improve the efficiency by 0.69%, is a thicker perovskite absorber (≈ 800 nm) (see Figure 4b). An optimal layer thickness improves single path absorption of incident low energy photons, ensuring that low energy photons can be readily absorbed and extracted, even if a rear transparent TCO contact is used. Poor absorption of low-energy photons is responsible for the decreased near bandgap signal in the EQE of simulated and experimental devices (as shown in Figures 3b and 4c) when compared to optimal simulated devices. Various studies have already demonstrated the feasibility of such high thicknesses in perovskite absorbers while maintaining high charge carrier mobility.^[24,51–53] Finally, replacing the front MgF_2 antireflection coating with micro-textures will improve the PCE by 0.73% (see Figure 4c). Micro-textures increase the probability of light in-coupling by allowing multiple reflections at the textured surface and increase the optical path length through the absorber.^[23,54–64] These textures also reduce the angular dependency in a tandem device compared to devices without a texture by minimizing the angular reflectance spectra for light incident from -60° to 60° , increasing in-coupled light.^[59,65] Such textures are typically formed in laboratory settings through UV nanoimprint lithography of a polydimethylsiloxane-based material^[23,58,61,63,66] which may be unsuitable for long-term outdoor use, although they have shown to be stable in real-world conditions for 32 day periods.^[66] However, textured glass substrates are an existing product capable of achieving similar optical effects, and are expected to be stable and scalable. As mentioned previously, we performed additional simulations to determine if shifting the perovskite

bandgap to the expected optimum while maintaining the optoelectronic quality will grant a notable boost to performance for an optically optimized device. This shift is expected to grant a further 0.3% maximum achievable PCE (see Figure 3d). Further details regarding these optical simulations can be found in the experimental section.

4. Conclusion

Perovskite-based 4T tandem solar cells have evolved significantly since their first introduction. Although there has been an enormous progress, significant room for improvement remains. Various studies have independently investigated methods for improving the performance of 4T tandem devices by improving the transmission of the semitransparent perovskite top subcell, including implementation of IO:H as a replacement for the front ITO, or the inclusion of ARCs. In this work, we employed a systematic approach to identify the potential and limits of current progress, replacing conventional ITO with high performance and high transmittance alternatives (IO:H and IZO) and adding independently optimized ARCs to achieve a PCE of 27.3% for perovskite/CIGS tandem solar cells in 4T configuration. Moreover, with the aid of simulations, we establish how to overcome the PCE limitations of our 4T perovskite/CIGS device. These simulations focus on the modification of our top semitransparent PSC, while maintaining our present perovskite composition, identifying architectural improvements that will allow further increased 4T perovskite/CIGS tandem solar cells PCE. By optimizing active layer thickness, employing index-matched encapsulated layers, and replacing the front ARC with a textured foil, we calculate our current stack is able to approach 30% PCE. A final set of simulations, aimed at modifying the bandgap of the top semitransparent PSC, indicate that for a completely optically optimized stack the difference in maximum achievable PCE between our 1.62 eV perovskite and a theoretical optimal 1.73 eV perovskite is only 0.3% absolute in PCE. This highlights that optical improvements are a more important optimization than bandgap in 4T perovskite/CIGS tandem solar cells.

5. Experimental Section

Materials: 2PACz (TCI, CAS: 20 999-38-6), lead iodide (PbI_2 : TCI, CAS: 10 101-63-0), formamidinium iodide (FAI: Dyenamo, CAS: 879 643-71-7), cesium chloride (abcr, CAS: 7647-17-8), 2-phenylethylammonium chloride (PEACl: Sigma-Aldrich; CAS: 156-28-5), bathocuproine (BCP: Lumtec, CAS: 4733-39-5), (MgF_2 : Sigma-Aldrich, CAS: 7783-40-6). All solvents including *N,N*-dimethylformamide, $\geq 99.9\%$ (DMF, CAS: 68-12-2), dimethyl sulfoxide (DMSO) anhydrous, $\geq 99.9\%$ CAS: 67-68-5), chlorobenzene (CB) anhydrous, 99.8%, CAS: 108-90-7), 2-Propanol, $\geq 98\%$, (IPA, CAS: 67-63-0) were ordered from Sigma-Aldrich. Ethanol absolute 99.8% was ordered from VWR Chemicals.

IO:H Substrate Fabrication: Front IO:H was deposited on clean glass using a Leybold Z600i inline sputtering system. The following sputtering parameters were used: DC power = 1.4 W cm^{-2} , pressure = 7.5 mTorr, 1.7% O_2 , and 3.4% H_2 in Ar. No intentional heating was applied during the deposition, post-deposition substrates were annealed for 20 min @ 250°C in vacuum.

Perovskite Solar Cell Fabrication: The planar p-i-n PSCs were fabricated with the architecture of: $MgF_2/\text{glass}/\text{ITO}$ or $\text{IO:H}/2\text{PACz}/\text{Cs}_{0.17}\text{FA}_{0.83}\text{Pb}(\text{I}_{0.92}\text{Br}_{0.08})_3/\text{C}_{60}/\text{SnO}_x/\text{IZO}/\text{MgF}_2$.

ITO (Luminescence Technology, CAS: 50 926-11-9) or IO:H substrates were cut in 0.16×0.16 cm and cleaned with acetone and isopropanol in an ultrasonic bath for 10 min each. The substrates were further treated with oxygen plasma for 3 min before the deposition of the HTL. A thin layer of 2PACz HTL was deposited on the ITO substrate by spin-coating at 3000 rpm for 30 s and subsequently annealed at 100 °C for 10 min. The 2PACz precursor solution was prepared by dissolving 2PACz in anhydrous ethanol with a concentration of 1 mmol L⁻¹. The prepared solution was put in an ultrasonic bath for 15 min before it was used. The double-cation perovskite precursor solution was prepared by dissolving 0.83 mmol FAI (143 mg), 0.17 mmol CsI (44 mg), 0.88 mmol PbI₂ (444 mg, 10% excess of PbI₂), and 0.12 mmol PbBr₂ (46 mg) in a 1 mL solvent mixture of DMF: DMSO at a 4:1 volume ratio. Afterward, 35 μL of PbCl₂:MACI solution with a molar ratio of 1:1 dissolved in 1 mL DMSO was added as a bulk passivation additive. The solution was deposited on top of the HTL by a two-step spin coating process: i) 1000 rpm (acceleration 2000 rpm s⁻¹) for 10 s, ii) 5000 rpm (acceleration 2000 rpm s⁻¹) for 40 s. 150 μL CB was actively deposited on the spinning substrate 20 s before the end of the second step. Samples were annealed at 100 °C for 30 min in an inert atmosphere.^[67] 1 nm thick LiF (passivation layer) and 20 nm C₆₀ (electron transport layer) were thermally evaporated at an evaporation rate of 0.1–0.2 Å/s at a pressure of around 10⁻⁶ mbar. Afterward, a 35 nm film of SnO_x was deposited over 300 cycles using the following settings: 1.6 s TDMAIn pulse time with a 12 s purge then 0.1 s water pulse time with a 16 s purge. A boosting system was utilized instead of the conventional bubbler due to the system layout. Under boosting, line flow was increased to 500 sccm immediately prior to pulsing to increase precursor concentration. This step is responsible for the abnormally high TDMAIn pulse time compared to other literature. Rear IZO was deposited using a Kurt J. Lesker PVD-75 thin-film deposition system. The following sputtering parameters were used to achieve 165 nm of IZO: RF power 100 W over 4 inch², deposition time = 2550 s, pressure = 1 mTorr, and O₂ to Ar ratio = 1%. To reduce the reflection losses, 125 and 150 nm thick MgF₂ were evaporated at the front and the rear side of the semitransparent perovskite solar cell.

Fabrication of CIGS Bottom Solar Cells: The CIGS solar cells were fabricated by co-evaporation of the elements in a classical multistage process which is described in detail in the earlier work.^[68] The cells comprised a metal grid and an anti-reflective MgF₂ coating on top, the designated area was 50 mm² (defined by mechanical scribing).

J–V Measurements: The perovskite and c-Si solar cells were characterized using a class AAA Newport solar simulator (xenon lamp). Thermal fabric was placed behind the measuring device, intended to provide thermal contact for temperature control and minimize reflection. For the CIGS solar cells, a class AAA Wacom WXS-90S-5, AM1.5G Super Solar Simulator (xenon lamp) was used. The solar simulator for the measurements of the PSCs was calibrated with a certified Si photodiode (Fraunhofer ISE) equipped with a KG5 bandpass filter. The J–V measurements were carried out under AM 1.5G conditions from V_{OC} to J_{SC} and J_{SC} to V_{OC} at a fixed rate of 600 mV s⁻¹ using a Keithley 2400 source meter. The stabilized PCE of the PSCs was determined by the power output at constant voltage close to the MPP under continuous AM 1.5G illumination for 5 min. The temperature (25 °C) of the PSCs was controlled actively using a Peltier element control circuit. The CIGS solar cell was measured either standalone or below the semitransparent perovskite filter fabricated along with the devices. The semitransparent PSCs were measured in a nitrogen atmosphere using an aperture mask with an area of 8.4 mm² to ensure a precisely defined active area, while the CIGS solar cell was measured without any mask (designated area 50 mm²).

EQE Measurements: EQE measurements were performed using a Bentham EQE system. A chopping frequency of ≈930 Hz with an integration time of 500 ms was used to obtain the spectra. The devices were not subjected to any pre-conditioning.

UV–vis Spectrophotometry: Transmittance and reflectance measurements were performed using a PerkinElmer Lambda 1050 spectrophotometer employed with an integrating sphere. The illumination spot was set as large as possible to average over possible slight in-homogeneities of the films.

Time-Resolved Photoluminescence Measurements: Time-resolved photoluminescence (TRPL) was carried out by a custom-built setup. A pulsed laser of 532 nm with a repetition rate of 1 kHz and a pulse width of 0.8 ns was used for the excitation of the samples. All measurements were performed with a pump fluence of ≈40 nJ cm⁻². The photoluminescence (PL) was captured using an ACTON spectrometer and a CCD camera PIMAX512 at room temperature. All PL measurements were carried out in air.

Simulations: The results of the simulations shown in Figure 4 were obtained using the open-source modeling platform EYcalc.^[69] An in-depth overview of this platform was presented in a previous publication.^[70] For the simulations performed in this work, we used the optics module to fit the EQE of the record experimental device and then to optimize the layer stack. Integrating the EQE over an AM1.5G spectrum, we then calculated the short-circuit current for each subcell. Finally, the PCE was computed via the electrics module, assuming the same electrical parameters at each optimization step.

Supporting Information

Supporting Information is available from the Wiley Online Library or from the author.

Acknowledgements

T.F., I.M.H., and S.G. contributed equally to this work. Financial support by the Initiating and Networking funding of the Helmholtz Association (HYIG of U.P. (VHNG-1148)), the Helmholtz Energy Materials Foundry (HEMF), PEROSEED (ZT0024), the German Federal Ministry for Economic Affairs and Climate Action (BMWK) through the project CAPITANO (03EE1038B). Furthermore, this project has received funding from the European Union's Horizon 2020 research and innovation program under grant agreement No 850937 (PERCISTAND).

Open Access funding enabled and organized by Projekt DEAL.

Conflict of Interest

The authors declare no conflict of interest.

Data Availability Statement

The data that support the findings of this study are available from the corresponding author upon reasonable request.

Keywords

CIGS, four-terminal, perovskites, photovoltaics, semitransparent perovskites, tandem solar cells

Received: July 20, 2022

Revised: September 8, 2022

Published online: October 9, 2022

[1] NREL, Best Research-Cell Efficiency Chart, <https://www.nrel.gov/pv/cell-efficiency.html> (accessed: September 2022).

[2] A. Al-Ashouri, A. Magomedov, M. Roß, M. Jošt, M. Talaikis, G. Chistiakova, T. Bertram, J. A. Márquez, E. Köhnen, E. Kasparavičius, S. Levenco, L. Gil-Escrig, C. J. Hages, R. Schlatmann, B. Rech, T. Malinauskas, T. Unold, C. A. Kaufmann, L. Korte, G. Niaura, V. Getautis, S. Albrecht, *Energy Environ. Sci.* **2019**, *12*, 3356.

- [3] A. Al-Ashouri, E. Köhnen, B. Li, A. Magomedov, H. Hempel, P. Caprioglio, J. A. Márquez, A. B. Morales Vilches, E. Kasparavicius, J. A. Smith, N. Phung, D. Menzel, M. Grisek, L. Kegelmann, D. Skroblin, C. Gollwitzer, T. Malinauskas, M. Jošt, G. Matič, B. Rech, R. Schlattmann, M. Topič, L. Korte, A. Abate, B. Stannowski, D. Neher, M. Stolterfoht, T. Unold, V. Getautis, S. Albrecht, *Science* **2020**, *370*, 1300.
- [4] M. A. Green, E. D. Dunlop, J. Hohl-Ebinger, M. Yoshita, N. Kopidakis, K. Bothe, D. Hinken, M. Rauer, X. Hao, *Prog. Photovoltaics Res. Appl.* **2022**, *30*, 687.
- [5] D. H. Kim, C. P. Muzzillo, J. Tong, A. F. Palmstrom, B. W. Larson, C. Choi, S. P. Harvey, S. Glynn, J. B. Whitaker, F. Zhang, Z. Li, H. Lu, M. F. A. M. van Hest, J. J. Berry, L. M. Mansfield, Y. Huang, Y. Yan, K. Zhu, *Joule* **2019**, *3*, 1734.
- [6] D. Yang, X. Zhang, Y. Hou, K. Wang, T. Ye, J. Yoon, C. Wu, M. Sanghadasa, S. (Frank) Liu, S. Priya, *Nano Energy* **2021**, *84*, 105934.
- [7] S. Gharibzadeh, I. M. Hossain, P. Fassel, B. A. Nejad, T. Abzieher, M. Schultes, E. Ahlswede, P. Jackson, M. Powalla, S. Schäfer, M. Rienäcker, T. Wietler, R. Peibst, U. Lemmer, B. S. Richards, U. W. Paetzold, *Adv. Funct. Mater.* **2020**, *30*, 1909919.
- [8] J. Tong, Q. Jiang, F. Zhang, S. B. Kang, D. H. Kim, K. Zhu, *ACS Energy Lett.* **2021**, *6*, 232.
- [9] M. A. Ruiz-Preciado, F. Gota, P. Fassel, I. M. Hossain, R. Singh, F. Laufer, F. Schackmar, T. Feeney, A. Farag, I. Allegro, H. Hu, S. Gharibzadeh, B. A. Nejad, V. S. Gevaerts, M. Simor, P. J. Bolt, U. W. Paetzold, *ACS Energy Lett.* **2022**, *7*, 2273.
- [10] S. Moghadamzadeh, I. M. Hossain, T. Duong, S. Gharibzadeh, T. Abzieher, H. Pham, H. Hu, P. Fassel, U. Lemmer, B. A. Nejad, U. W. Paetzold, *J. Mater. Chem. A* **2020**, *8*, 24608.
- [11] H. Hu, S. Moghadamzadeh, R. Azmi, Y. Li, M. Kaiser, J. C. Fischer, Q. Jin, J. Maibach, I. M. Hossain, U. W. Paetzold, B. Abdollahi Nejad, *Adv. Funct. Mater.* **2021**, *32*, 2107650.
- [12] B. Abdollahi Nejad, D. B. Ritzer, H. Hu, F. Schackmar, S. Moghadamzadeh, T. Feeney, R. Singh, F. Laufer, R. Schmager, R. Azmi, M. Kaiser, T. Abzieher, S. Gharibzadeh, E. Ahlswede, U. Lemmer, B. S. Richards, U. W. Paetzold, *Nat. Energy* **2022**, *7*, 620.
- [13] I. J. Park, J. H. Park, S. G. Ji, M. A. Park, J. H. Jang, J. Y. Kim, *Joule* **2019**, *3*, 807.
- [14] F. Gota, M. Langenhorst, R. Schmager, J. Lehr, U. W. Paetzold, *Joule* **2020**, *4*, 2387.
- [15] M. Langenhorst, B. Sautter, R. Schmager, J. Lehr, E. Ahlswede, M. Powalla, U. Lemmer, B. S. Richards, U. W. Paetzold, *Prog. Photovoltaics Res. Appl.* **2019**, *27*, 290.
- [16] M. Schultes, T. Helder, E. Ahlswede, M. F. Aygüler, P. Jackson, S. Paetel, J. A. Schwenzer, I. M. Hossain, U. W. Paetzold, M. Powalla, *ACS Appl. Energy Mater.* **2019**, *2*, 7823.
- [17] C. D. Bailie, M. G. Christoforo, J. P. Mailoa, A. R. Bowering, E. L. Unger, W. H. Nguyen, J. Burschka, N. Pellet, J. Z. Lee, M. Grätzel, R. Noufi, T. Buonassisi, A. Salleo, M. D. McGehee, *Energy Environ. Sci.* **2015**, *8*, 956.
- [18] R. Sheng, A. W. Y. Ho-Baillie, S. Huang, M. Keevers, X. Hao, L. Jiang, Y.-B. Cheng, M. A. Green, *J. Phys. Chem. Lett.* **2015**, *6*, 3931.
- [19] F. Fu, T. Feurer, T. Jäger, E. Avancini, B. Bissig, S. Yoon, S. Buecheler, A. N. Tiwari, *Nat. Commun.* **2015**, *6*, 8932.
- [20] J. Werner, L. Barraud, A. Walter, M. Bräuninger, F. Sahli, D. Sacchetto, N. Tétreault, B. Paviet-Salomon, S.-J. Moon, C. Allebé, M. Despeisse, S. Nicolay, S. De Wolf, B. Niesen, C. Ballif, *ACS Energy Lett.* **2016**, *1*, 474.
- [21] T. Duong, Y. Wu, H. Shen, J. Peng, X. Fu, D. Jacobs, E.-C. Wang, T. C. Kho, K. C. Fong, M. Stocks, E. Franklin, A. Blakers, N. Zin, K. McIntosh, W. Li, Y.-B. Cheng, T. P. White, K. Weber, K. Catchpole, *Adv. Energy Mater.* **2017**, *7*, 1700228.
- [22] F. Fu, T. Feurer, T. P. Weiss, S. Pisoni, E. Avancini, C. Andres, S. Buecheler, A. N. Tiwari, *Nat. Energy* **2017**, *2*, 16190.
- [23] H. Shen, T. Duong, J. Peng, D. Jacobs, N. Wu, J. Gong, Y. Wu, S. K. Karuturi, X. Fu, K. Weber, X. Xiao, T. P. White, K. Catchpole, *Energy Environ. Sci.* **2018**, *11*, 394.
- [24] B. Chen, S. Baek, Y. Hou, E. Aydin, M. De Bastiani, B. Scheffel, A. Proppe, Z. Huang, M. Wei, Y. Wang, E. Jung, T. G. Allen, E. Van Kerschaver, F. P. García de Arquer, M. I. Saidaminov, S. Hoogland, S. De Wolf, E. H. Sargent, *Nat. Commun.* **2020**, *11*, 1257.
- [25] M. Jaysankar, B. A. L. Raul, J. Bastos, C. Burgess, C. Weijtens, M. Creatore, T. Aernouts, Y. Kuang, R. Gehlhaar, A. Hadipour, J. Poortmans, *ACS Energy Lett.* **2019**, *4*, 259.
- [26] Two world-records for 4T perovskite tandem, <https://www.solliance.eu/2021/two-world-records-for-4t-perovskite-tandem/> (accessed: March 2022).
- [27] C. Zhang, M. Chen, F. Fu, H. Zhu, T. Feurer, W. Tian, C. Zhu, K. Zhou, S. Jin, S. M. Zakeeruddin, A. N. Tiwari, N. P. Padture, M. Grätzel, Y. Shi, *Energy Environ. Sci.* **2022**, *15*, 1536.
- [28] I. M. Hossain, Y. J. Donie, R. Schmager, M. S. Abdelkhalik, M. Rienäcker, T. F. Wietler, R. Peibst, A. Karabanov, J. A. Schwenzer, S. Moghadamzadeh, U. Lemmer, B. S. Richards, G. Gomard, U. W. Paetzold, *Opt. Express* **2020**, *28*, 8878.
- [29] A. Belghachi, N. Limam, *Chinese J. Phys.* **2017**, *55*, 1127.
- [30] F. Lang, M. Jošt, K. Frohna, E. Köhnen, A. Al-Ashouri, A. R. Bowman, T. Bertram, A. B. Morales-Vilches, D. Koushik, E. M. Tennyson, K. Galkowski, G. Landi, M. Creatore, B. Stannowski, C. A. Kaufmann, J. Bundesmann, J. Rappich, B. Rech, A. Denker, S. Albrecht, H.-C. Neitzert, N. H. Nickel, S. D. Stranks, *Joule* **2020**, *4*, 1054.
- [31] Y. Jiang, Y. Qi, *Mater. Chem. Front.* **2021**, *5*, 4833.
- [32] a De Vos, *J. Phys. D. Appl. Phys.* **1980**, *13*, 839.
- [33] G. E. Eperon, M. T. Hörantner, H. J. Snaith, *Nat. Rev. Chem.* **2017**, *1*, 0095.
- [34] M. H. Futscher, B. Ehrler, *ACS Energy Lett.* **2016**, *1*, 863.
- [35] R. Hosseini Ahangharnejhad, A. B. Phillips, K. Ghimire, P. Koirala, Z. Song, H. M. M. Barudi, A. Habte, M. Sengupta, R. J. Ellingson, Y. Yan, R. W. Collins, N. J. Podraza, M. J. Heben, *Sustain. Energy Fuels* **2019**, *3*, 1841.
- [36] D. A. Jacobs, M. Langenhorst, F. Sahli, B. S. Richards, T. P. White, C. Ballif, K. R. Catchpole, U. W. Paetzold, *J. Phys. Chem. Lett.* **2019**, *10*, 3159.
- [37] M. Jaysankar, M. Filipič, B. Zielinski, R. Schmager, W. Song, W. Qiu, U. W. Paetzold, T. Aernouts, M. Debucquoy, R. Gehlhaar, J. Poortmans, *Energy Environ. Sci.* **2018**, *11*, 1489.
- [38] T. Duong, N. Lal, D. Grant, D. Jacobs, P. Zheng, S. Rahman, H. Shen, M. Stocks, A. Blakers, K. Weber, T. P. White, K. R. Catchpole, *IEEE J. Photovoltaics* **2016**, *6*, 679.
- [39] M. Schultes, Ph.D. thesis, Karlsruhe Institut für Technologie (KIT) **2020**, <https://doi.org/10.5445/IR/1000118573>.
- [40] I. M. Hossain, Ph.D. thesis, Karlsruhe Institut für Technologie (KIT) **2021**, <https://doi.org/10.5445/IR/1000130563>.
- [41] D. P. McMeekin, G. Sadoughi, W. Rehman, G. E. Eperon, M. Saliba, M. T. Horantner, A. Haghighirad, N. Sakai, L. Korte, B. Rech, M. B. Johnston, L. M. Herz, H. J. Snaith, M. T. Hörantner, A. Haghighirad, N. Sakai, L. Korte, B. Rech, M. B. Johnston, L. M. Herz, H. J. Snaith, *Science* **2016**, *351*, 151.
- [42] J. Werner, G. Dubuis, A. Walter, P. Löper, S.-J. Moon, S. Nicolay, M. Morales-Masis, S. De Wolf, B. Niesen, C. Ballif, *Sol. Energy Mater. Sol. Cells* **2015**, *141*, 407.
- [43] H. Scherg-Kurmes, S. Seeger, S. Körner, B. Rech, R. Schlattmann, B. Szyszka, *Thin Solid Films* **2016**, *599*, 78.
- [44] T. Koida, M. Kondo, K. Tsutsumi, A. Sakaguchi, M. Suzuki, H. Fujiwara, *J. Appl. Phys.* **2010**, *107*, 033514.
- [45] T. Koida, H. Fujiwara, M. Kondo, *Jpn. J. Appl. Phys.* **2007**, *46*, L685.

- [46] S. H. Brewer, S. Franzen, *J. Phys. Chem. B* **2002**, *106*, 12986.
- [47] T. S. Sathiaraj, *Microelectronics J.* **2008**, *39*, 1444.
- [48] M. J. Dodge, *Appl. Opt.* **1984**, *23*, 1980.
- [49] M. Stolterfoht, P. Caprioglio, C. M. Wolff, J. A. Márquez, J. Nordmann, S. Zhang, D. Rothhardt, U. Hörmann, Y. Amir, A. Redinger, L. Kegelmann, F. Zu, S. Albrecht, N. Koch, T. Kirchartz, M. Saliba, T. Unold, D. Neher, *Energy Environ. Sci.* **2019**, *12*, 2778.
- [50] X. Liu, H. Yu, L. Yan, Q. Dong, Q. Wan, Y. Zhou, B. Song, Y. Li, *ACS Appl. Mater. Interfaces* **2015**, *7*, 6230.
- [51] J. Chen, L. Zuo, Y. Zhang, X. Lian, W. Fu, J. Yan, J. Li, G. Wu, C.-Z. Li, H. Chen, *Adv. Energy Mater.* **2018**, *8*, 1800438.
- [52] L. Zhu, Y. Xu, P. Zhang, J. Shi, Y. Zhao, H. Zhang, J. Wu, Y. Luo, D. Li, Q. Meng, *J. Mater. Chem. A* **2017**, *5*, 20874.
- [53] A. Farag, R. Schmager, P. Fassel, P. Noack, B. Wattenberg, T. Dippell, U. W. Paetzold, *ACS Appl. Energy Mater.* **2022**, *5*, 6700.
- [54] A. Deinega, I. Valuev, B. Potapkin, Y. Lozovik, *J. Opt. Soc. Am. A* **2011**, *28*, 770.
- [55] B. Lipovsek, J. Krc, M. Topic, *IEEE J. Photovoltaics* **2018**, *8*, 783.
- [56] B. Lipovsek, J. Krc, M. Topic, *IEEE J. Photovoltaics* **2014**, *4*, 639.
- [57] B. W. Schneider, N. N. Lal, S. Baker-Finch, T. P. White, *Opt. Express* **2014**, *22*, A1422.
- [58] R. Schmager, B. Fritz, R. Hünig, K. Ding, U. Lemmer, B. S. Richards, G. Gomard, U. W. Paetzold, *ACS Photonics* **2017**, *4*, 2687.
- [59] S. Dottermusch, R. Schmager, E. Klampafitis, S. Paetel, O. Kiowski, K. Ding, B. S. Richards, U. W. Paetzold, *Prog. Photovoltaics Res. Appl.* **2019**, *27*, 593.
- [60] M. Jošt, E. Köhnen, A. B. Morales-Vilches, B. Lipovšek, K. Jäger, B. Macco, A. Al-Ashouri, J. Krč, L. Korte, B. Rech, R. Schlatmann, M. Topič, B. Stannowski, S. Albrecht, *Energy Environ. Sci.* **2018**, *11*, 3511.
- [61] S. Esiner, T. Bus, M. M. Wienk, K. Hermans, R. A. J. Janssen, *Adv. Energy Mater.* **2013**, *3*, 1013.
- [62] B. Lipovšek, A. Čampa, F. Guo, C. J. Brabec, K. Forberich, J. Krč, M. Topič, *Opt. Express* **2017**, *25*, A176.
- [63] J. D. Myers, W. Cao, V. Cassidy, S.-H. Eom, R. Zhou, L. Yang, W. You, J. Xue, *Energy Environ. Sci.* **2012**, *5*, 6900.
- [64] C. Ulbrich, A. Gerber, K. Hermans, A. Lambertz, U. Rau, *Prog. Photovoltaics Res. Appl.* **2013**, *21*, 1672.
- [65] S.-Y. Kuo, M.-Y. Hsieh, H.-V. Han, F.-I. Lai, T.-Y. Chuang, P. Yu, C.-C. Lin, H.-C. Kuo, *Opt. Express* **2014**, *22*, 2860.
- [66] J. W. Leem, J. S. Yu, *RSC Adv.* **2015**, *5*, 60804.
- [67] S. Gharibzadeh, P. Fassel, I. M. Hossain, P. Rohrbeck, M. Frericks, M. Schmidt, T. Duong, M. R. Khan, T. Abzieher, B. A. Nejjand, F. Schackmar, O. Almora, T. Feeney, R. Singh, D. Fuchs, U. Lemmer, J. P. Hofmann, S. A. L. Weber, U. W. Paetzold, *Energy Environ. Sci.* **2021**, *14*, 5875.
- [68] P. Jackson, R. Wuerz, D. Hariskos, E. Lotter, W. Witte, M. Powalla, *Phys. Status Solidi RRL* **2016**, *10*, 583.
- [69] R. Schmager, U. W. Paetzold, M. Langenhorst, F. Gota, J. Lehr, *Zenodo* **2021**, <https://doi.org/10.5281/zenodo.4696257>.
- [70] R. Schmager, M. Langenhorst, J. Lehr, U. Lemmer, B. S. Richards, U. W. Paetzold, *Opt. Express* **2019**, *27*, A507.